

A Study on Hot Tearing in Direct Chill Casting of Al-Mn-Mg Alloys Using a Multi-scale Approach

N. Khodaei

A.B. Phillion

Keywords: Hot tearing, DC casting, Multi-scale simulation, Semi-solid, Solidification

This article has been published in Metallurgical and Materials Transactions B. The final publication is available at Springer via <https://doi.org/10.1007/s11663-021-02108-7>

Abstract

A multi-scale approach for simulating hot tearing during the DC casting of aluminum alloys is presented. The novelty of this approach lies in the combination of a macro-scale finite element simulation of the DC casting process with direct prediction of hot tears via a meso-scale multi-physics granular model. This approach is capable of simulating hot tearing initiation, growth, and propagation within a representative volume element of the mushy zone. The change of cooling conditions experienced by the DC cast billet as a result of variations in casting speed as well as non-uniformity of heat extraction from different locations of the billet affect the deformation state, cooling rate, and thermal gradient, which further influence the strain rate, grain size, permeability, and feeding coefficient. Considering all the mentioned parameters, the multi-scale approach emphasizes the fact that hot tearing is a phenomenon resulting from the combination of the tensile deformation and restricted feeding of the mushy zone. The developed hot tearing formation maps identify the locations where hot tearing will occur as predicted by the multi-scale approach for two alloys - AA5182 and AA3104 - thus demonstrating the approach's sensitivity to both processing parameters and alloy composition.

I. Introduction

Over the past few years, computer-based modeling has provided a valuable means to improve the DC casting process of aluminum alloys in terms of process optimiza-

tion and prediction of defects. As the computational power increases, more process details can be simulated (1). One of the most severe and unrecoverable defects encountered in DC casting operations, which has attracted considerable interest by industry and researchers, is hot tearing. This defect is attributed to the combination of limited feedability of the mushy zone with deformation of the semi-solid skeleton at high solid fraction (2) and has been widely investigated by various methods both experimentally and numerically. The experimental studies are limited due to the high temperature at which hot tears form and the sensitivity of factors that cause hot tearing to the casting geometry. As a result, the trend toward implementing computer simulations rather than conducting experimental studies is increasing.

There are several parameters critical to the formation of hot tearing in DC casting. Alloy chemistry determines the grain morphology and its size which directly affect hot tearing propensity (3). Many studies suggested that grain refinement has a positive impact on hot tearing resistance in general. The study conducted by Warrington et al. (4) on DC cast aluminum 7050 and 7010 alloys showed that the addition of grain refiners changes the grain structure from columnar to equiaxed-dendritic grains and consequently decreases hot cracking vulnerability. However, by adding too much grain refiner, more cracks appeared, which was explained to be due to the decrease in the permeability of the mushy zone (5). It has been also demonstrated that the microstructure in which the primary grains are surrounded by thicker eutectic phase exhibits more hot tearing resistance (6) since the eutectic phase improves healing phenomenon or in other words the liquid feeding between the grain (7). The amount of alloying elements have a significant impact on the freezing range of binary alloys and as it becomes larger the alloy spends a longer time in susceptible regions, which increases hot tearing tendency (2). The most important processing parameters affecting hot tearing tendency are casting speed, melt temperature, and cooling water flow rate since all these parameters influence melt flow and cooling conditions, which affect the stress induced by thermal contraction and solidification shrinkage. Most researchers have agreed that in aluminum alloys, high melt temperature increases the thermal gradient during the solidification, which promotes the growth of columnar dendritic grains with lower hot tearing resistance compared to equiaxed globular grains (8; 9). Larger casting speed

provides higher solidification rate and deeper mushy zone; both increase the chance of hot tearing initiation (10). High cooling water flow rate causes uneven thermal contraction, meaning that the surface cools down faster than the center which leads to accumulation of stresses and strains and consequently hot tearing development (11).

From the available hot tearing criteria in the literature, it is noted that most only qualitatively predict hot tearing, i.e. they cannot predict whether or not a crack actually forms. This is because the criteria are not able to directly predict the distribution of strain and localization of feeding at the grain boundaries, which both strongly influence the hot tearing phenomenon (12). Therefore, the main concern of the casting industry, i.e. quantitative prediction of hot tearing formation, remains.

In the mushy zone, where both solid and liquid coexist, a great variety of grains having different morphologies (columnar dendritic, equiaxed dendritic, and globular) can nucleate and grow. The distribution of grain morphology, and localized nature of grain boundaries, must be taken into account to improve defect prediction (13). Recently, researchers have proposed the use of multi-physics models that can directly investigate the simultaneous effect of both deformation and fluid flow on the solidification behavior at the mesoscopic scale. In this regard, different granular mechanics approaches have been suggested to link the semi-solid mechanical behavior of a domain with equiaxed globular microstructure to the evolution of solid-liquid interface and fluid flow as a result of deformation and shrinkage.

In an early model, Lahaie and Bouchard (14) used an idealized 2-D microstructure to simulate the response of a semi-solid to an applied strain rate taking into account liquid feeding. In this model, the solidification of all grains occurred at the same rate; all solid grains were in the shape of hexagons and the intergranular liquid was distributed uniformly between the grains before the deformation was applied. Although the authors claimed that the results of their model are in agreement with experimental observations, in reality, the solidification of grains is neither at the same rate nor in 2 dimensions. More recently Vernède et al. (15) developed a 2-D granular model that simulates the mechanical behavior of the mushy zone within a random arrangement of grains created via a Voronoi tessellation. This model was capable of simulating the grain structure at a given solid fraction, localization of fluid flow and the forces caused

by liquid feeding and deformation. Despite the progress made by 2-D techniques that take into account the random distribution of grains, the description of solidification process in the scale of grains remained imperfect due to the 3-D nature of both semi-solid deformation and fluid flow between the grains (16). To address this need, Sistaninia et al. (17) developed a meso-scale 3-D granular hydro-mechanical model that predicts the constitutive behavior of a semi-solid considering fluid flow between the grains, percolation, bridging of the solid grains and hot tearing formation. In this model, it was assumed that equiaxed solid grains surrounded by liquid films are randomly distributed in a representative volume element. Comparing X-ray images taken during the experimental trial with the simulation results, Sistaninia et al. concluded that the model offers a good insight into the prediction of hot tearing (18; 19).

In order to utilize the meso-scale 3-D granular hydro-mechanical model developed by Sistaninia to directly predict hot tearing during DC casting, knowledge of the thermal and mechanical fields experienced by the casting is required. Such data can only be acquired by modelling the thermal conditions and corresponding stress and strain evolution during the DC casting process. In this study a macro-scale thermomechanical model for the DC casting of aluminum alloys (20), which is capable of predicting the evolution of stress, strain, strain rate, temperature, etc. at different locations of the casting for different casting speeds, is coupled with Sistaninia's meso-scale model to demonstrate a multi-scale approach for quantifying the severity of hot tears and predict where they occur in the DC cast billet. This research thus develops a bridge linking the macro- and the meso- scale models and explains how the two models are coupled together in order to quantify hot tearing predictions. The model is applied to two important wrought aluminum alloys, AA5182 and AA3104. In the next section, the methodology used to investigate the problem of hot tearing in DC casting of aluminum alloys will be presented. Henceforward, Sistaninia's meso-scale model and the thermomechanical model of the DC casting process will be called "the meso-scale model" and "the macro-scale model", respectively.

II. Numerical Methods

The flow chart of the coupling procedure between the thermal and mechanical fields provided by the macro-scale model with the semi-solid cracking predictions provided by the meso-scale model is presented in Fig. 1. A pore fraction model (21) is used to identify the locations within the DC billet where hot tears are most likely to form.

a. The Meso-scale Model

The meso-scale model is an in-house C++ software developed by Sistaninia and colleagues (17; 22). The model consists of four separate modules: (1) the solidification module to create the solid-liquid geometry at any solid fraction, (2) the fluid flow module for simulating liquid pressure within the intergranular channels, (3) the semi-solid deformation module to model the semi-solid mechanical behavior, and finally (4) the failure module to simulate crack initiation and propagation. Since hot tearing formation is the result of both a lack of liquid feeding and deformation of the alloy in the semi-solid region, the fluid flow, semi-solid deformation, and failure modules are coupled together. The input geometry for the solidification module is created using the open source library Voro++. For the fluid flow calculations, a purpose-written finite element code solves the assumed Poiseuille Flow problem. The semi-solid deformation simulations are performed using the commercial finite element package ABAQUS (v.2019). The mesh of the solid grains and fluid channels is created from the output of the solidification module. Finally, by considering a failure criterion, the fluid flow, semi-solid deformation, and failure modules are coupled through the pressure in the liquid and opening at the grain boundaries. Through the use of a control file that specifies the input parameters, simulation of the meso-scale model, which takes into account the simultaneous effect of fluid flow between the grains and deformation on hot tearing, can be performed. The output of this model is the simulated tensile behavior of an RVE with constant grain size and solid fraction. The reader is referred to Refs (18), (23), and (22), respectively, for additional information on each of the sub-modules of the meso-scale model.

To simulate semi-solid deformation via the meso-scale model, proper fluid and mechanical boundary conditions must be assigned to all surfaces of the RVE. Fig. 2 (a)

shows a schematic of an RVE at solid fraction of 0.98. In terms of mechanical boundary conditions, (1) the surface $x = L_x$ is joined to a reference node, which is displaced at a constant bulk strain rate taken from the macro-scale model; (2) symmetry planes are assigned to the surfaces $x = 0$, $y = 0$, and $z = 0$; and (3) the surfaces $z = L_z$ and $y = L_y$ are free to move. In terms of fluid flow, a Robin boundary condition is imposed on the surface $x = 0$ in order to account for the fact that the liquid feeding the semi-solid RVE must take into account all the flow through the mushy zone to reach that point. This is expressed as:

$$q_l = F(p_l - p_m), \quad (1)$$

where q_l is the microscopic flux ($\mu\text{m}\cdot\text{s}^{-1}$), F is the feeding coefficient, p_l is the liquid pressure and p_m is the metallostatic pressure. It has been shown by Sistaninia et al. (18) that F can be defined as:

$$F = \frac{q_l}{p_l - p_m} = \frac{1}{\int_{T_l}^T \frac{\mu_l(1-g_s(T))}{K(g_s)G} dT}, \quad (2)$$

where μ_l is the liquid viscosity, G is the thermal gradient, g_s is the solid fraction, and K is the permeability of the mushy zone. The remaining surfaces of the RVE are considered to be closed to fluid flow.

b. The Macro-scale Model

The DC casting process of a round billet (320 mm diameter \times 800 mm length) is simulated in the general purpose finite element (FE) software package ABAQUS version 2019 using an axisymmetric geometry as shown in Fig. 2 (b). To simplify the problem, the interactions of the billet with the mold and the bottom block are taken into account by applying relevant boundary conditions. 2-D coupled temperature-displacement elements, 4 mm in height \times 5 mm in width, are used to mesh the computational domain. The increase in the casting height as a result of the downward movement of the bottom block is simulated such that the bottom block and the billet remain in a fixed position and the billet height grows in vertical direction by addition of horizontal layers incrementally. Accordingly, the thermal boundary condition is moving upward at a rate consistent with the casting speed. To calculate the evolution

of stress, strain, and temperature as a function of position in the billet and time, the solidification and constitutive models are implemented through a user subroutine.

Two alloys have been studied in this research. The first is an aluminum AA5182 alloy (Al-0.35Mn-4.5Mg, wt.%) (20), which has a large non-equilibrium freezing range ($\Delta T = 130^\circ\text{C}$) (24). The second is an aluminum AA3104 alloy (Al-0.88Mn-1.15Mg, wt.%) (25), which has a shorter freezing range ($\Delta T = 70^\circ\text{C}$) (24). In a comprehensive study by Lin et al. (26), the hot tearing susceptibility of these two alloys were ranked as AA5182 < AA3104. Moreover, grain refinement has been found to be highly effective in reducing hot tearing susceptibility in AA5182 but less so in AA3104. This last point is attributed to the large freezing range of AA5182.

In order to solve the heat transfer equations during casting, it is necessary to specify initial thermal conditions as well as proper heat transfer coefficients with the environment. The initial temperatures are set to 650°C and 670°C , which are the typical pouring temperatures of AA5182 and AA3104, respectively, while the ambient temperature is assumed to be 25°C . The details on different thermal heat transfer coefficients on surfaces Γ_1 - Γ_5 are described in Ref. (20). It is also necessary to apply mechanical boundary conditions to avoid convergence issues associated with rigid body motion. For this purpose, an axisymmetric boundary condition is applied to the axis of rotation ($x = 0$) to restrict the deformation of the centerline in radial direction. In addition, the bottom node at the centreline of the billet is constrained in radial (x) and axial (y) directions to suppress the separation of the bottom block and the billet at the centerline.

Finally, to perform a fully coupled thermo-mechanical analysis, a complete set of temperature-dependent thermal and mechanical properties are required. With respect to semi-solid deformation and hot tearing, the liquidus temperature (T_{liq}), the mechanical coalescence temperature (T_{coh}), and the solidus temperature (T_{sol}) are critical. Including the mechanical coalescence temperature in the calculations is of importance in order to identify the point at which the semi-solid material starts developing strength and exhibits contraction. The temperature for mechanical coalescence was considered to be 602°C for AA5182, and 620°C for AA3104. More information on the applied thermophysical properties of the AA5182 and AA3104 alloys and constitutive models used to describe the inelastic behavior of the billet are provided in Refs. (20; 25). Since

a constitutive model which can predict the behavior of AA3104 alloy above solidus temperature and input to the macro-scale model was not available in the literature, the model proposed by Phillion et al. for AA5182 alloy was used (27).

c. Identifying regions of high hot tearing susceptibility

The simulation output of the macro-scale model provides the evolution in temperature, cooling rate, thermal gradient, grain size, and different states of stress and strain. However, such outputs do not tell anything about hot tearing tendencies. Therefore, a hot tearing criterion is required to predict regions at risk of hot tearing formation. The thermal and mechanical conditions experienced by these regions will then be transferred to the meso-scale model to quantify the occurrence of a hot tear.

The hot tearing criterion used in this work is the pore fraction hot tearing model first proposed by Monroe and Beckermann (28), and later developed by Dou and Phillion (21). This model is based on the idea, beyond a critical solid fraction, i.e. $g_{s,cr} = 0.98$, fluid flow ceases and thus all the shrinkage and deformation must cause porosity thus increasing hot tearing susceptibility. The amount of porosity as a result of deformation, called “deformation pore fraction” can be defined in two directions, i.e. parallel ($f_{p,de,\epsilon x}$) and perpendicular to the thermal gradient ($f_{p,de,\epsilon y}$) as shown below:

$$f_{p,de,\epsilon x} = \frac{\dot{\epsilon}_{px}\Delta T_f}{\dot{T}} \int_0^{g_{l,cr}} (1 - g_l) \frac{d\theta}{dg_l} dg_l, \quad (3)$$

$$f_{p,de,\epsilon y} = \frac{\dot{\epsilon}_{py}\Delta T_f}{\dot{T}} \int_0^{g_{l,cr}} (1 - g_l) \frac{d\theta}{dg_l} dg_l; \quad (4)$$

where $g_{l,cr} = 1 - g_{s,cr}$ is the critical liquid fraction, $\dot{\epsilon}_{py}$ is the strain rate perpendicular to the thermal gradient, $\dot{\epsilon}_{px}$ is the strain rate parallel with the thermal gradient, ΔT_f is the freezing range, \dot{T} is the cooling rate, and θ equals $\frac{T - T_{sol}}{\Delta T_f}$. By applying the pore fraction hot model, the pore fraction distribution and hence the hot tearing susceptibility during the DC casting process is calculated.

d. Multi-scale Approach to Hot Tearing

To implement the multi-scale approach by utilizing the tools outlined above, the following steps as outlined in Fig. 1 are taken:

1. Using the macro-scale model, the temperature and stress/strain evolution during DC casting is predicted.
2. The cooling rate, strain rate parallel to the thermal gradient and strain rate perpendicular to the thermal gradient are output from the macro-scale model at $g_{l,cr}$ corresponding to $T = 546^\circ\text{C}$ and $T = 591^\circ\text{C}$ for AA5182 and AA3104, respectively, via a Python script run in ABAQUS.
3. The distribution of pore fraction in the DC cast billet are calculated using the output of the previous step. With this knowledge, the locations most susceptible to hot tearing are identified.
4. Additional characteristics of locations having the highest hot tearing susceptibility, i.e. grain size (d), thermal gradient (G), and bulk strain rate ($\dot{\epsilon}_v$), are extracted from the macro-scale model and used as input parameters by the meso-scale model to simulate semi-solid tensile behavior and consequently predict the occurrence of hot tears.
5. Hot tearing maps, which show the locations within the DC casting billets where hot tears occur with respect to the multi-scale approach for different macro-scale simulations, are generated.

Please note that: (1) The grain size d is estimated following Easton et al.'s approach (29) that considers the cooling rate (\dot{T}), grain refiner addition ($[\text{TiB}_2]$), and alloy composition as controlling parameters:

$$d(\mu\text{m}) = \frac{1}{1.4(1 - e^{-0.569\dot{T}^{0.685}})[\text{TiB}_2]^{1/3}} + (281 + \frac{381}{\dot{T}^{0.5}}) \frac{1}{Q}; \quad (5)$$

where \dot{T} is calculated from the macro-scale simulation at a temperature just below T_{liq} , it is assumed that the alloys are grain-refined with 0.005 wt.% $[\text{TiB}_2]$, and the effect of alloy composition is quantified through the growth restriction factor ($Q = \sum_i m_i c_{0,i} (k_i - 1)$ with m_i being the liquidus gradient, $c_{0,i}$ the composition, and k_i the binary partition coefficient for each element i in the alloy). (2) The thermal gradient is calculated from the temperature field evolution given by the macro-scale simulation, at a temperature just above T_{sol} . (3) The bulk strain rate $\dot{\epsilon}_v$ is calculated as $3 \times \dot{\epsilon}_{px}$.

III. Results and Discussion

Three different macro-scale simulations, each using a different casting speed (Case A - $66 \text{ mm}\cdot\text{min}^{-1}$; Case B - $56 \text{ mm}\cdot\text{min}^{-1}$; Case C - $46 \text{ mm}\cdot\text{min}^{-1}$), were performed for both of the studied alloys. Since the main challenge in this coupling is to determine when and how to apply the meso-scale model to optimize the computational costs, first, the results of the pore fraction model for the three simulation cases for AA5182 are presented in Section ???. Then, the characteristics of the locations in the AA5182 macro-scale simulations exhibiting the highest susceptibility to hot tearing with respect to the pore fraction model are discussed in Section ???. After that, in Section ???, the focus is placed on examining the tensile behavior of the AA5182 meso-scale RVEs possessing characteristics of the locations with the highest risk of hot tearing based on the pore fraction model. Finally, the hot tearing maps for AA5182 and AA3104 obtained from the multi-scale approach are compared and discussed against the available hot tearing models in the literature.

a. Hot Tearing Susceptibility as Predicted by the Macro-scale Model

In order to explore hot tearing susceptibility of AA5182 during DC casting, the distributions of the total deformation pore fraction ($f_{p,de} = f_{p,de,\epsilon x} + f_{p,de,\epsilon y}$) for simulation cases A, B, and C are analyzed. Fig. 3 shows the variation of the total deformation pore fraction as a function of distance from the bottom block along the centerline of the billet at $g_{s,cr}$ for all three cases. As can be seen, the pore fraction is an increasing function of the distance from the bottom block until it reaches a peak value at a few millimetres above the bottom surface of the billet, which indicates the susceptibility of the billet to hot tearing in the start-up region. As the casting speed increases, the peak value of the deformation pore fraction also increases and shifts to lower heights in the billet such that it occurs at the height of 12 mm, 16 mm, and 24 mm above the bottom block for Cases A, B, and C, respectively. After the peak value has been attained, the pore fraction shows a decreasing trend until 50-100 mm above the bottom block depending on the casting speed. For case C, the pore fraction becomes zero above 90 mm from the bottom block, meaning that there is no vulnerability to hot tearing; however, for case A and B, the pore fraction starts to increase after 80 and 100 mm above

the bottom block, respectively in such a way that for case A at the height of 350 mm, it even becomes larger than the peak value. The finding that hot tearing susceptibility increases above approx. 80 mm from the bottom block contradicts with industry experience where there is little risk of hot tearing in the steady state regime (30).

As shown in Eq. 3 and Eq. 4, the pore fractions $f_{p,de,\epsilon x}$ and $f_{p,de,\epsilon y}$ are strong functions of $\dot{\epsilon}_{px}$ and $\dot{\epsilon}_{py}$. Fig. 4 (a) and (b) show the variation in the strain rate parallel ($\dot{\epsilon}_{px}$) and perpendicular ($\dot{\epsilon}_{py}$) to the thermal gradient along the centerline of the billet as a function of the distance from the bottom block. By comparing the two figures, it is noted that the evolution of the deformation pore fraction in the start-up and the steady state regimes is controlled by $\dot{\epsilon}_{px}$ and $\dot{\epsilon}_{py}$, respectively. Therefore, the increase in the deformation pore fraction for case A in the steady state region is the result of the increase in $\dot{\epsilon}_{py}$ as shown in Fig. 4 (b), which implies higher hot tearing susceptibility in the steady state region. However, as shown in Fig. 5, the total strain perpendicular to the thermal gradient along the centerline of the billet becomes negative above 32 mm from the bottom block, meaning that the strain is compressive which not only does not cause cracking, but can also heal small hot tears by pushing liquid into regions where feeding is difficult.

In order to study the hot tearing propensity in the radial direction, the evolution of deformation pore fraction as a function of distance from the centerline of the billet for cases A, B, and C at three different heights of 12 mm, 16 mm, and 24 mm above the bottom block is plotted in Fig. 6. For each case, the height is chosen based on the location of the peak value in Fig. 3. It can be observed that the deformation pore fraction generally decreases as one approaches the surface of the billet, implying that the hot tearing susceptibility decreases in radial direction. Therefore, from the results of applying the pore fraction hot tearing criterion to the macro-scale model, it can be concluded that there is a risk of hot tearing formation near the center of the billet and as the casting speed increases, the distance between the point with the highest vulnerability to hot tearing and the bottom surface of the billet decreases. Moreover, there is no risk of hot tearing near the surface of the billet.

b. Characteristics of Susceptible Locations

Although the risk of hot tearing initiation has been investigated so far, the question whether or not hot tears will initiate still remains. To answer this question, it is required to identify the location within the billet demonstrating the highest risk of hot tearing formation according to the pore fraction model for each simulation case. Such locations, listed in Table 1 are named X, Y, and Z for the AA5182 simulation cases A, B, and C. At these locations, the grain size, strain rate, and thermal gradient are extracted from the macro-scale model and used as inputs, along with the corresponding feeding coefficient F , to create the meso-scale simulations for the AA5182 alloy. The values for each simulation are listed in Table 2.

Fig. 7 plots the above-mentioned parameters as a function of position along the billet's radius at the critical heights above the bottom block from Table 1 in order to gain an understanding of their variation in a DC cast billet. Beginning with Fig. 7 (a) the grain size is shown to decrease towards the surface of the billet, as expected due to the higher thermal gradients, Fig. 7 (b). The effect of casting speed is seen to be negligible except right near the billet's surface. The bulk strain and strain rate are defined as the volumetric deformation and the rate of such deformation. However, the strain rate parallel to the thermal gradient that causes cracking in the start-up region as explained by the pore fraction model, is an axial strain rate. Fig. 7 (c) plots the bulk strain rate $\dot{\epsilon}_v$ in the radial direction assuming that this quantity can be calculated as $3 \times \dot{\epsilon}_{px}$. It can be seen that the bulk strain rate increases with the casting speed and decreases in radial direction. Finally, Fig. 7 (d) shows the variation in F with solid fraction for thermal gradients of 2500, 3500, and 5500 K.m⁻¹ assuming a constant viscosity of 0.0015 Pa.s and a grain size of 220 μ m. As can be seen, as the solid fraction increases and the thermal gradient decreases, the feedability of the mushy zone decreases.

c. Meso-scale Model Predictions of Semi-solid Deformation

With the model inputs shown in Table 2, the meso-scale model can be applied for the AA5182 alloy. Figs. 8 (a) and (b) represent the average stress and the average liquid pressure of the RVE as a function of strain over the surface $x = L_x$ at $g_{s,cr}$ for locations X, Y, and Z. As can be seen in Fig. 8 (a), the stress increases with the strain for all three

locations until it reaches a maximum value, which can be called the failure stress, then no further increase is observed in the stress evolution. Moreover, the strain at which the failure is achieved varies in such a way that for X it is almost twice as large as that for Z. However, the failure stress does not considerably vary for these three locations.

As illustrated in Fig. 8 (b), by applying tensile deformation to the RVE, the liquid pressure decreases from an initial value that is assumed to be zero. For each location, the strain at which the maximum liquid pressure drop and the maximum stress are achieved represents the onset of cracking. For location Z, the crack initiation happens at a smaller strain but larger liquid pressure drop in comparison to locations X and Y. This can be explained in terms of the smaller feeding coefficient (F) used for Z, which causes more restricted liquid feeding between the grains and consequently a larger pressure drop as the deformation proceeds. However, since the strain rate for each simulation case is different, it is not possible to give a clear statement about the effect of liquid feeding and also strain rate on the tensile behavior of the RVE.

To more clearly demonstrate the tensile behavior of the RVE, contour maps of the maximum principal strain at three strain values ($\epsilon_1 = 0.0133$, $\epsilon_2 = 0.0163$ and $\epsilon_3 = 0.0174$; markers (a), (b), and (c) in Fig. 8 (a), are shown in Fig. 9 (a),(b), and (c). In Fig. 9 (a), which is one increment before the maximum stress, the strain is localized between the grains, but there is no sign of a crack. Crack initiation and growth are clearly visible in Fig. 9 (b) and (c), which correspond to one and two increments after the maximum stress is obtained. The increase in the liquid pressure after the maximum pressure drop is reached is due to the fact that the crack growth causes the associated liquid channels to become dry and its remaining liquid is sucked into other regions of the RVE. The corresponding liquid channels are then eliminated from the fluid flow and deformation calculations.

Fig. 10 plots the stress-strain behaviour of five meso-scale model simulations for the AA5182 alloy with a constant grain size of $220 \mu\text{m}$ in order to investigate the effects of bulk strain rate ($\dot{\epsilon}_v$) and the feeding coefficient (F) on the tensile behavior of the mushy zone. As can be seen, the decrease in F and increase in $\dot{\epsilon}_v$ results in a higher resistance to tensile deformation or in other words higher stiffness. However, determining which parameter controls the tensile behavior of the RVE depends on their

values. A comparison between the green curve ($F = 0.01 \mu\text{m.Pa}^{-1}.\text{s}^{-1}$, $\dot{\epsilon}_v = 0.0017 \text{ s}^{-1}$) and the blue curve ($F = 0.007 \mu\text{m.Pa}^{-1}.\text{s}^{-1}$, $\dot{\epsilon}_v = 0.0012 \text{ s}^{-1}$) indicates that $\dot{\epsilon}_v$ is the controlling parameter, while comparing the green curve with the red curve ($F = 0.007 \mu\text{m.Pa}^{-1}.\text{s}^{-1}$, $\dot{\epsilon}_v = 0.0015 \text{ s}^{-1}$) shows the opposite. With this information, F is thus the controlling parameter in Fig. 8 (a), meaning that although $\dot{\epsilon}_v$ increases with casting speed, the increase in F results in lower stiffness for location X.

Although the grain size was almost constant for the three locations X, Y, and Z at $220 \mu\text{m}$ (see Table 2), it generally varies with location in the billet as shown in Fig. 7 (a). To study the role of grain size, a number of meso-scale simulations were performed considering a constant $F = 0.007 \mu\text{m.Pa}^{-1}.\text{s}^{-1}$ and various $\dot{\epsilon}_v$ and d with the results summarized in the contour map shown in Fig. 11. It is worth mentioning that large values for $\dot{\epsilon}_v$ were used deliberately to force cracks to form within the RVE. It is clear that the stress at fracture decreases with grain size. However, for a constant grain size, the variation in $\dot{\epsilon}_v$ does not significantly affect the stress at fracture. This observation is consistent with the results given in Fig. 8 (a). Hence, it can be deduced that regardless of the applied bulk strain rate, as the grain size decreases (e.g. via grain refining), the crack initiation requires a larger stress which implies lower propensity to hot tearing formation.

d. Quantitative Prediction of Hot Tearing

As explained so far, the multi-scale approach can provide detailed knowledge of the mechanical behavior of the mushy zone at different locations and consequently predict crack initiation and growth considering the liquid pressure drop between the grains as a result of deformation. This approach can be used to generate a Hot Tearing Map for AA5182 that defines locations within a DC cast billet where hot tearing formation most likely occurs. To create such a map, the data required for the meso-scale model was extracted from all nodes from the macro-scale model. First, nodes having lower strain rates, higher feeding coefficients, and smaller grain sizes than the three sets of conditions shown in Table 2 that resulted in hot tearing formation were eliminated from the list. Second, the meso-scale simulation was carried out for the remaining nodes. The resulting hot tearing formation maps generated for the macro-scale simulation cases A,

B, and C can be seen in Fig. 12 (a1), (b1), and (c1); the red dots represent locations in the macro-scale simulation domain in which hot tears were predicted to occur by the meso-scale model. As can be seen, and as expected, larger casting speeds result in an increase in the number of red points.

But, is this approach sensitive to alloy composition? As outlined in Section 2, a similar macro-scale model was created for the AA3104 alloy. This has a shorter freezing range than AA5182, but is known to be quite sensitive to hot tearing; perhaps because early grain coherency due to large grains prevents the flow of interdendritic liquid into the central dendritic network. Fig. 12 (a2), (b2), and (c2) show the Hot Tearing Maps for this alloy, also with casting speeds of $66 \text{ mm}\cdot\text{min}^{-1}$, $56 \text{ mm}\cdot\text{min}^{-1}$, and $46 \text{ mm}\cdot\text{min}^{-1}$. Although AA3104 has a smaller freezing range, It can be seen that for a constant casting speed the number of locations identified as "hot tear predicted" is much higher in this alloy as compared to AA5182. Therefore, it can be inferred that a combination of different parameters affects hot tearing formation. In terms of process parameters, the main difference is the pouring temperature, as the macro-scale simulation for AA3104 used a value of 670°C , which is 20°C larger than for AA5182. The effect of alloy composition is seen through the growth restriction factor resulting in a much larger grain size for AA3104 than for AA5182. The higher hot tearing susceptibility of AA3104 in comparison to AA5182 as predicted by the multi-scale approach is in agreement with the observations of Lin et al. (26), which underlines the importance of the grain size for hot tearing susceptibility in casting of an alloy with large nonequilibrium freezing range and the grain size above $200 \mu\text{m}$.

IV. Summary

A multi-scale approach for simulating hot tearing during the DC casting of aluminum alloys has been presented for two alloys, AA5182 and AA3104. The novelty of this approach lies in the combination of the macro-scale simulation of the DC casting process with the direct prediction of hot tears via a meso-scale multi-physics granular model. This approach is capable of simulating hot tearing initiation, growth, and propagation within a representative volume element of the mushy zone as a function of alloy

composition. The change of cooling condition experienced by the DC cast billet as a result of the variation of casting speed as well as non-uniformity of heat extraction from different locations of the billet affect the deformation state, cooling rate, and thermal gradient, which further influence the strain rate, grain size, permeability, and feeding coefficient. Considering all the mentioned parameters, the multi-scale approach emphasizes the fact that hot tearing is a phenomenon resulting from the combination of the tensile deformation and restricted feeding of the mushy zone. The developed hot tearing formation maps demonstrate the locations where hot tearing will occur as predicted by the multi-scale approach; these maps are sensitive to both alloy composition and processing parameters. The predictions are in good agreement with the results of prior experimental and numerical investigations (e.g. M’Hamdi et al. (31), Jamaly et al. (20), and Lin et al. (26)), that have shown that hot tearing susceptibility increases with an increase in the casting speed and grain size. Finally, it should be noted that the accuracy of the multi-scale approach highly depends on the availability of the thermophysical properties and constitutive equations explaining the alloy’s behavior in the semi-solid region.

V. Acknowledgements

The authors wish to thank the Natural Sciences and Engineering Research Council of Canada (NSERC) for financial support.

VI. Tables

Table 1: Locations within the billet for which the semi-solid geometries are generated for the AA5182 alloy; x is the distance from the centerline and y is the distance from the bottom block.

Simulation case	Identifier	x (mm)	y (mm)
A ($66 \text{ mm}\cdot\text{min}^{-1}$)	X	15	12
B ($56 \text{ mm}\cdot\text{min}^{-1}$)	Y	15	16
C ($46 \text{ mm}\cdot\text{min}^{-1}$)	Z	20	24

Table 2: Characteristics of nodes demonstrating the highest deformation pore fraction at solid fraction of 0.98 for the AA5182 alloy

Simulation case	X	Y	Z
d (μm)	220	220	220
$\dot{\epsilon}_v$ (s^{-1})	0.0017	0.0015	0.0012
G ($\text{K}\cdot\text{m}^{-1}$)	3000	2850	2700
F ($\mu\text{m}\cdot\text{Pa}^{-1}\cdot\text{s}^{-1}$)	0.008	0.007	0.006

VII. Figure Headings

Figure 1: Flow chart of the multi-scale approach.

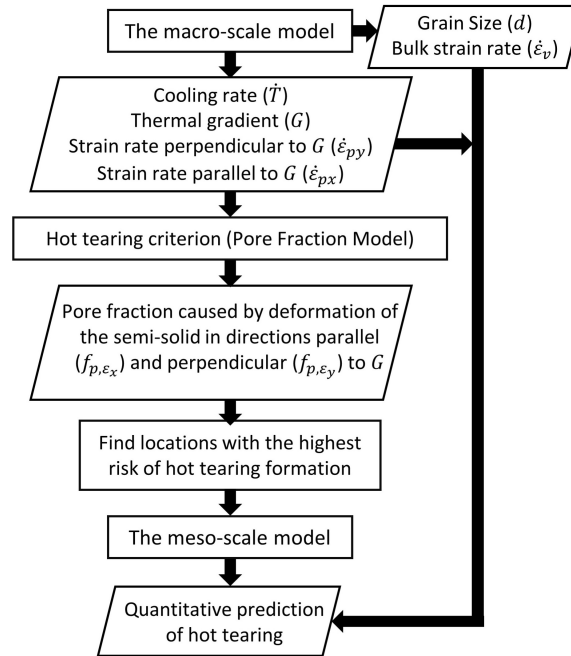


Figure 2: Schematic of (a) the computational domain in the macro-scale model, (b) a representative volume element (RVE) at $g_s = 0.98$.

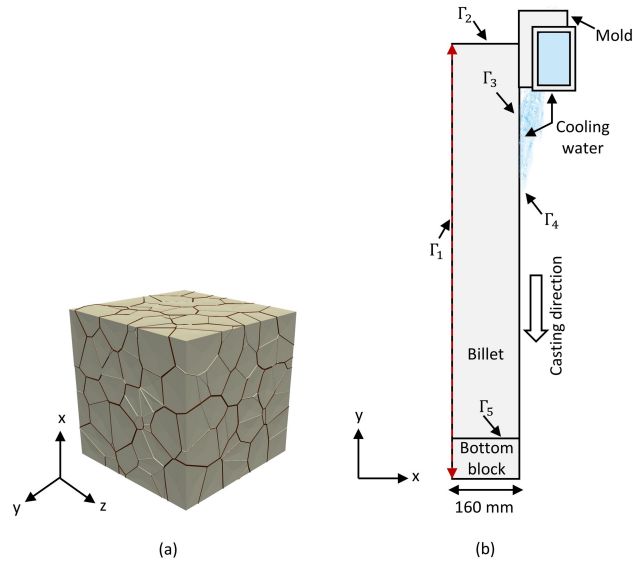


Figure 3: Evolution of the deformation pore fraction along the centerline of the billet at solid fraction of 0.98 for the AA5182 macro-scale simulation cases A, B, and C.

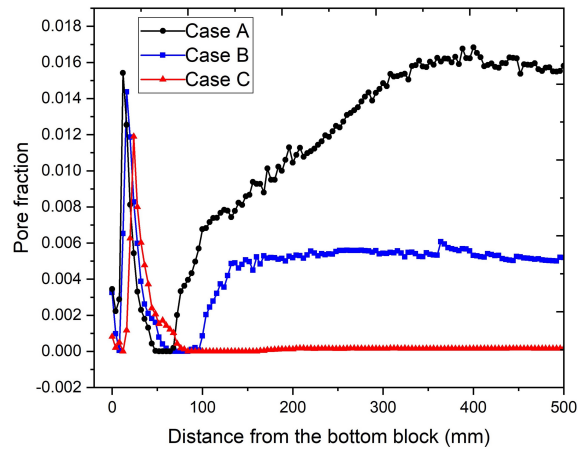
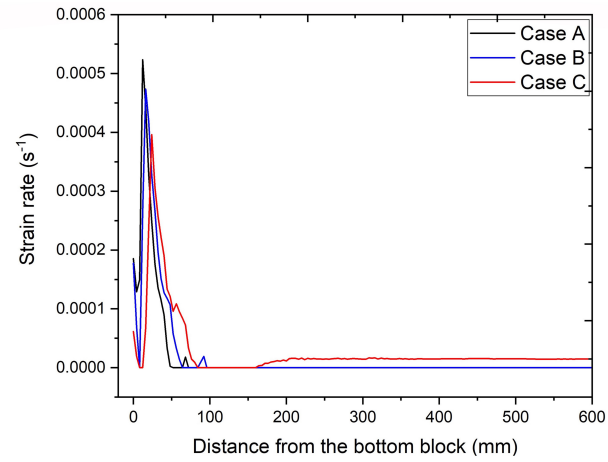
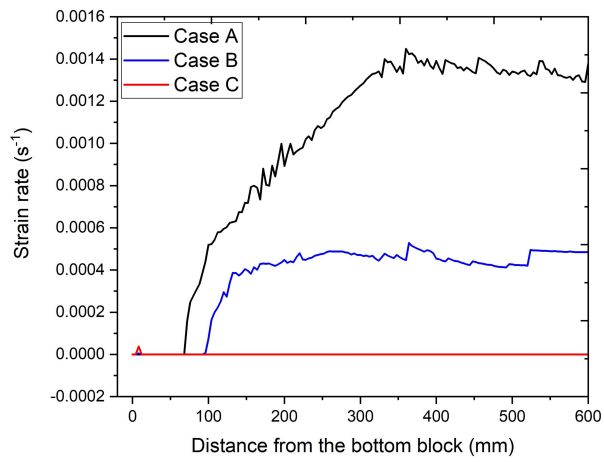


Figure 4: Evolution of (a) the strain rate parallel with the thermal gradient ($\dot{\epsilon}_{px}$), and (b) the strain rate perpendicular to the thermal gradient ($\dot{\epsilon}_{py}$) along the centerline of billet at solid fraction of 0.98 for the AA5182 macro-scale simulation cases A, B, and C.



(a)



(b)

Figure 5: Variation in the strain perpendicular to the thermal gradient as a function of distance from the bottom block along the centerline of the billet at solid fraction of 0.98 for the AA5182 macro-scale simulation cases A, B, and C.

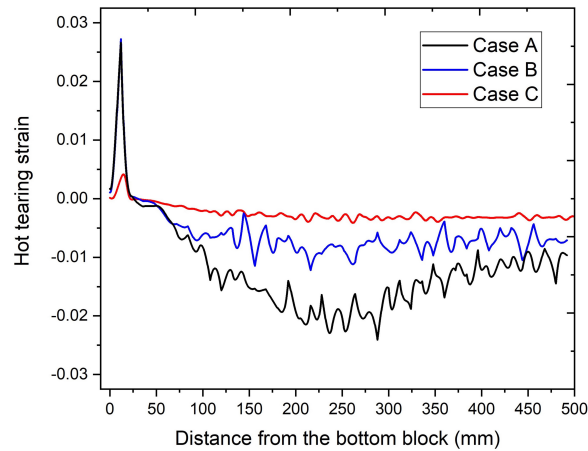


Figure 6: Evolution of the deformation pore fraction as a function of distance from the centerline of the billet at solid fraction of 0.98 for the AA5182 macro-scale simulation cases A, B, and C.

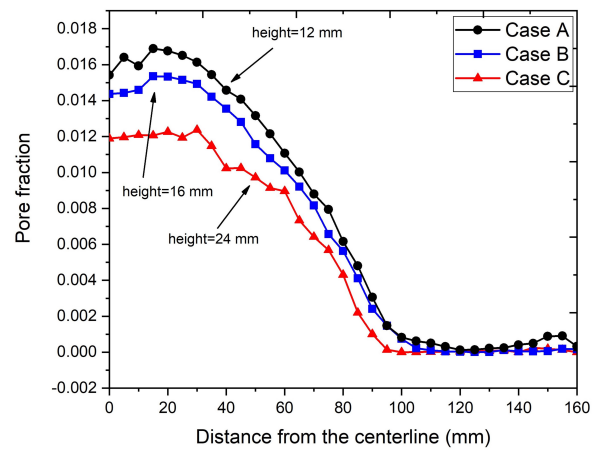


Figure 7: Evolution of (a) grain size, (b) thermal gradient, and (c) bulk strain rate ($\dot{\epsilon}_v$) in the radial direction at $g_{s,cr}$ at the critical heights from the AA5182 macro-scale simulation cases A, B, and C, (d) variation in feeding coefficient F with solid fraction for thermal gradients of 2500 K.m^{-1} , 3500 K.m^{-1} , 5500 K.m^{-1} and a constant grain size of $220 \mu\text{m}$.

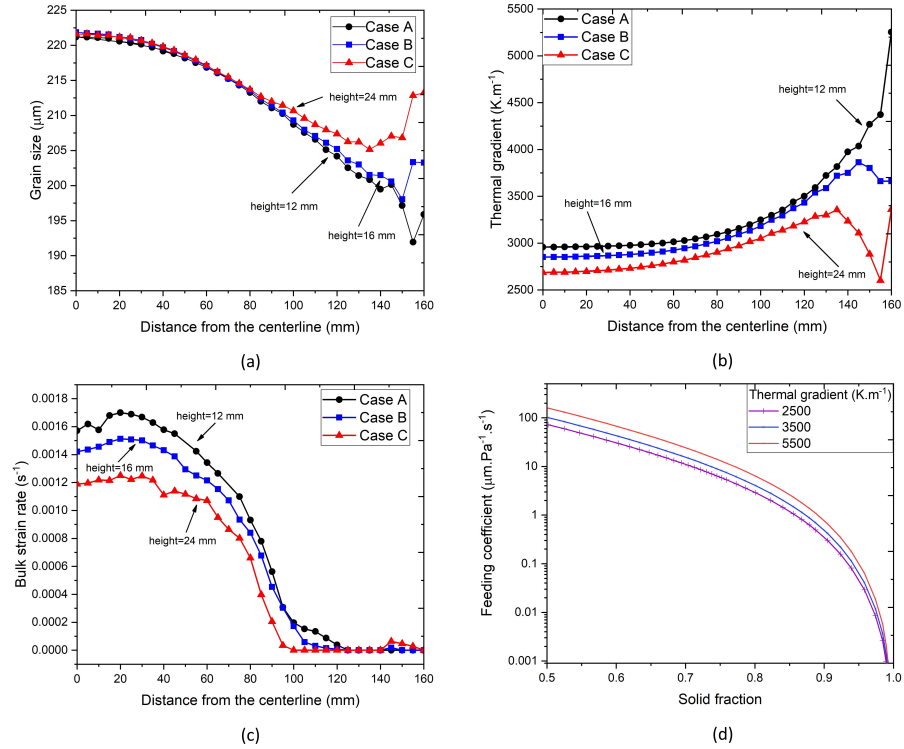


Figure 8: Simulated (a) stress-strain curves and (b) pressure-strain curves of the RVE with liquid feeding for locations X, Y, and Z from the AA5182 macro-scale simulations. The blue squares (a), (b), and (c) correspond to strain values of 0.0133, 0.0163 and 0.0174, respectively.

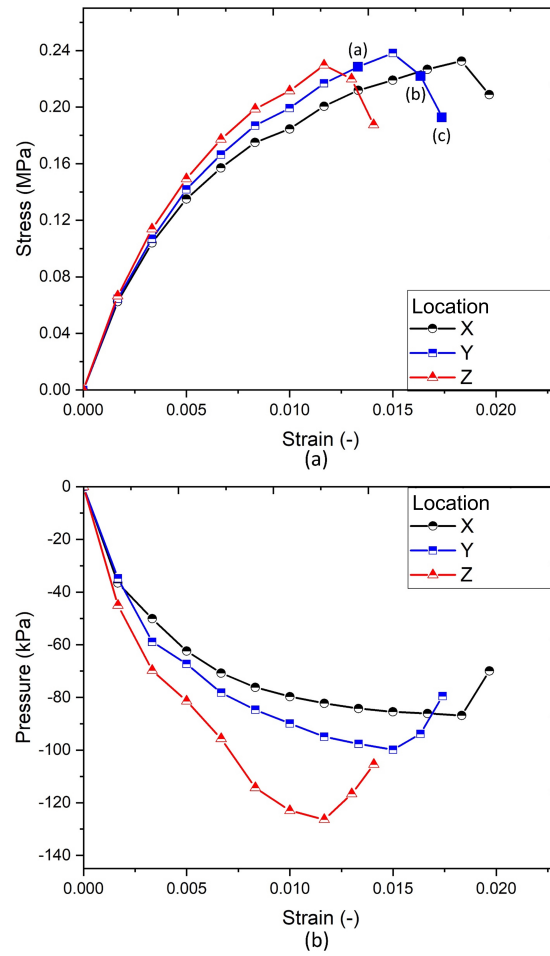


Figure 9: Contour maps of maximum principal strain for three strain values of (a) $\varepsilon_1 = 0.0133$, (b) $\varepsilon_2 = 0.0163$, and (c) $\varepsilon_3 = 0.0174$, as defined in Fig. 8 (a) corresponding to the AA5182 location Y.

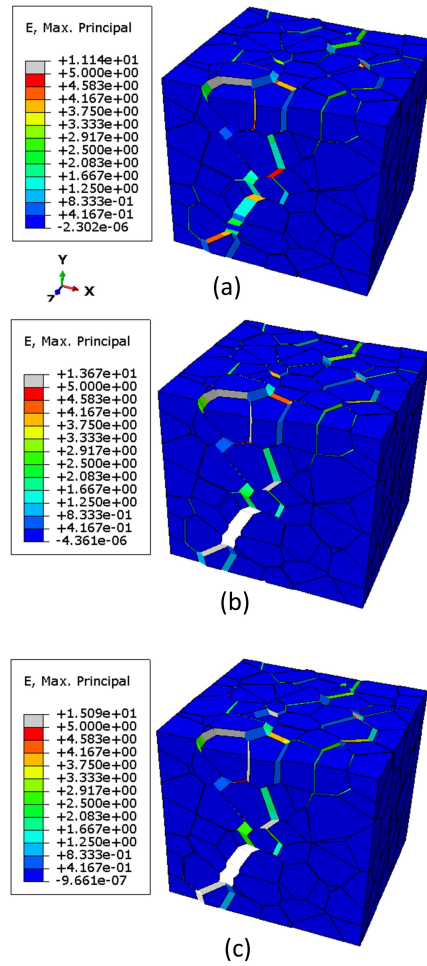


Figure 10: Simulated stress-strain behavior of a meso-scale model RVE for various (arbitrary) feeding coefficients and bulk strain rates.

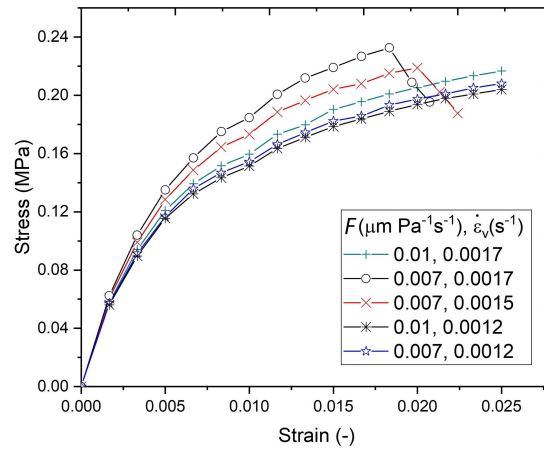


Figure 11: Contour map of stress at fracture over a range of bulk strain rates and grain sizes for $F=0.007 \mu\text{m}\cdot\text{Pa}^{-1}\cdot\text{s}^{-1}$.

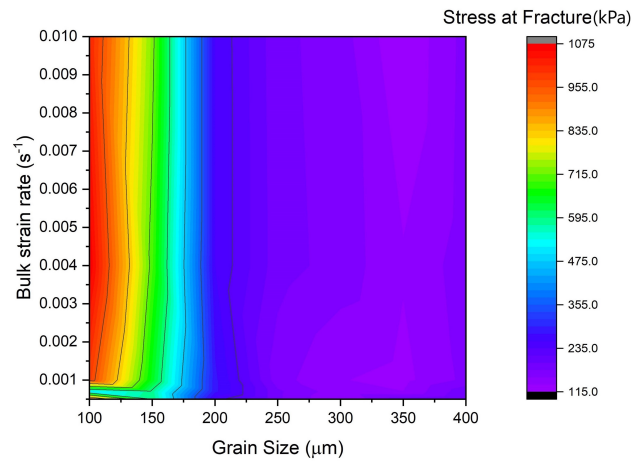
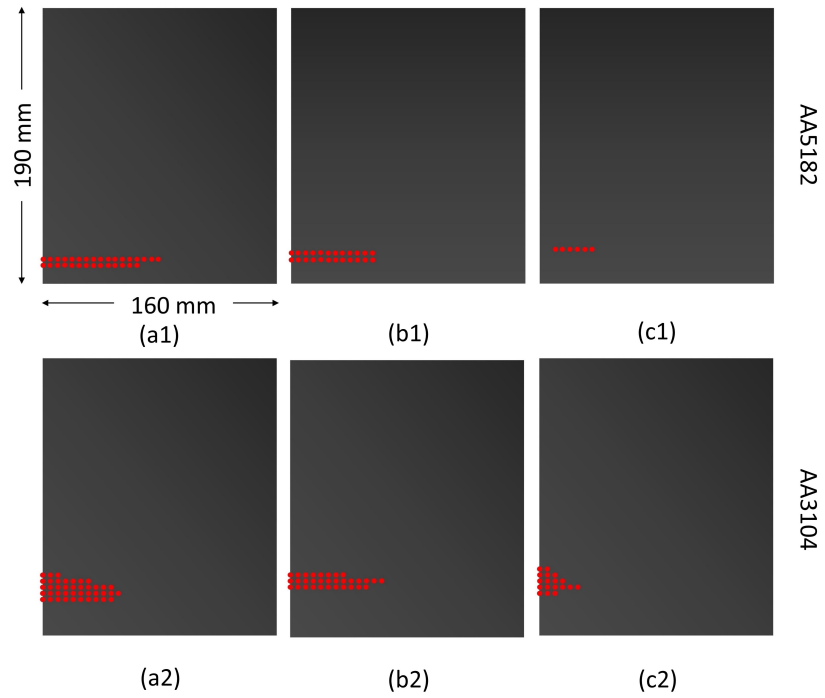


Figure 12: Hot tearing formation map of AA5182 and AA3104 alloys for simulation cases (a) A with casting speed of $66 \text{ mm}\cdot\text{min}^{-1}$, (b) B with casting speed of $56 \text{ mm}\cdot\text{min}^{-1}$, and (c) C with casting speed of $46 \text{ mm}\cdot\text{min}^{-1}$.



VIII. References

- [1] B.G. Thomas, M. Bellet. Modeling of stress, distortion, and hot tearing (2008)
- [2] S. Li, D. Apelian, International Journal of Metalcasting **5**(1), 23 (2011)
- [3] J. Verö, The Metals Industry **48**, 431 (1936)
- [4] D. Warrington, D. McCartney, Cast metals **3**(4), 202 (1990)
- [5] J.F. Grandfield, C.J. Davidson, J.A. Taylor, Continuous Casting pp. 245–250 (2000)
- [6] R. Rosenberg, M. Flemings, H. Taylor, AFS Trans **69**, 518 (1960)
- [7] M. Easton, J.F. Grandfield, D.H. StJohn, B. Rinderer, in *Materials science forum*, vol. 519 (Trans Tech Publ, 2006), vol. 519, pp. 1675–1680
- [8] W. Kool, L. Katgerman, et al., in *Materials Science Forum*, vol. 396 (Trans Tech Publications Ltd., Zurich-Uetikon, Switzerland, 2002), vol. 396, pp. 179–184
- [9] C.W. Briggs, *The metallurgy of steel castings* (McGraw-Hill book Company, Incorporated, 1946)
- [10] J.M. Drezet, M. Rappaz, G.U. Grün, M. Gremaud, Metallurgical and Materials Transactions A **31**(6), 1627 (2000)
- [11] J. Sengupta, B. Thomas, M. Wells, Metallurgical and Materials Transactions A **36**(1), 187 (2005)
- [12] S. Vernede, P. Jarry, M. Rappaz, Acta Materialia **54**(15), 4023 (2006)
- [13] M. Rappaz, Current Opinion in Solid State and Materials Science **20**(1), 37 (2016)
- [14] D. Lahaie, M. Bouchard, Metallurgical and materials Transactions B **32**(4), 697 (2001)
- [15] S. Vernède, J.A. Dantzig, M. Rappaz, Acta Materialia **57**(5), 1554 (2009)

- [16] J.M. Drezet, M. Sistaninia, M. Rappaz, *Matériaux & Techniques* **98**(4), 261 (2010)
- [17] M. Sistaninia, A. Phillion, J.M. Drezet, M. Rappaz, in *IOP Conference Series: Materials Science and Engineering*, vol. 33 (IOP Publishing, 2012), vol. 33, p. 012070
- [18] M. Sistaninia, A. Phillion, J.M. Drezet, M. Rappaz, *Acta materialia* **60**(9), 3902 (2012)
- [19] S. Terzi, L. Salvo, M. Suéry, N. Limodin, J. Adrien, E. Maire, Y. Pannier, M. Bornert, D. Bernard, M. Felberbaum, et al., *Scripta Materialia* **61**(5), 449 (2009)
- [20] N. Jamaly, A. Phillion, J.M. Drezet, *Metallurgical and Materials Transactions B* **44**(5), 1287 (2013)
- [21] R. Dou, A. Phillion, *Metallurgical and Materials Transactions A* **47**(8), 4217 (2016)
- [22] M. Sistaninia, A. Phillion, J.M. Drezet, M. Rappaz, *Acta Materialia* **60**(19), 6793 (2012)
- [23] M. Sistaninia, A. Phillion, J.M. Drezet, M. Rappaz, *Metallurgical and Materials Transactions A* **42**(1), 239 (2011)
- [24] A. Phillion, S. Thompson, S. Cockcroft, M. Wells, *Materials Science and Engineering: A* **497**(1-2), 388 (2008)
- [25] A. Alankar, M.A. Wells, *Materials Science and Engineering: A* **527**(29-30), 7812 (2010)
- [26] S. Lin, C. Aliravci, M. Pekguleryuz, *Metallurgical and Materials Transactions A* **38**(5), 1056 (2007)
- [27] A. Phillion, S. Cockcroft, P. Lee, *Modelling and Simulation in Materials science and Engineering* **17**(5), 055011 (2009)

- [28] C. Monroe, C. Beckermann, *Jom* **66**(8), 1439 (2014)
- [29] M.A. Easton, D.H. StJohn, *Materials Science and Engineering: A* **486**(1-2), 8 (2008)
- [30] J.M. Drezet, D. Allehaux, in *Hot cracking phenomena in welds II* (Springer, 2008), pp. 27–45
- [31] M. M'hamdi, S. Benum, D. Mortensen, H. Fjaer, J.M. Drezet, *Metallurgical and Materials Transactions A* **34**(9), 1941 (2003)